nature communications

Article

https://doi.org/10.1038/s41467-026-73152-7

Insolation-forced oceanic changes triggered the Eurasian Ice Sheet collapse and the Last Termination

Received: 5 December 2024

Accepted: 30 April 2026

Published online: 14 May 2026

Check for updates

Dong Wu[1,2], Siqi Li[3], Jón Eiríksson[4], Esther Ruth Guðmundsdóttir[4], Yair Rosenthal[5], Ningjing Hu[2,6], Dejiang Fan[1], Yanguang Liu[2,6] ✉ & Xu Zhang[3,7] ✉

The collapse of Northern Hemisphere ice sheets has been deemed as a trigger of positive climate feedback during Quaternary glacial terminations. Increasing boreal summer insolation is widely considered the primary driver; however, the precise initiating mechanisms remain elusive. Here we report an unambiguous warming trend in the southern Nordic Seas since the late Last Glacial Maximum, coinciding with the marked increase in 65°N summer insolation, and subsequently followed by a distinct surface cooling linked to intense freshwater discharge. Our reconstructions indicate that the initial collapse during the Last Termination began within the Eurasian Ice Sheet. Increasing boreal insolation weakened the latitudinal insolation gradient and displaced the westerlies northward, promoting poleward oceanic heat transport and ensuing warming in the Nordic Seas. This warming accelerated the disintegration of marine-terminating glaciers of the Eurasian Ice Sheet, leading to a catastrophic meltwater release. The resulting freshwater perturbation contributed to the early weakening of the Atlantic Meridional Overturning Circulation and ultimately triggered the destabilization of the Laurentide Ice Sheet, further accelerating the deglaciation process.

Quaternary glacial cycles have been closely linked to the changes of Earth's orbital parameters[1,2], characterized by a long cooling period ending with a relatively short warming interval marked by a significant reduction of ice sheets, a sawtooth pattern variation consistent with boreal summer insolation changes[3,4]. Identifying the processes that triggered these rapid collapses of ice sheets, also known as "glacial terminations", is essential for understanding the mechanisms of glacial cycles[5]. A commonly discussed hypothesis attributes the onset of terminations to the peaks of surface air temperature induced by the insolation maxima[6], leading to rapid surface melt which reduced ice thickness and enhancing the subglacial lubrication and sliding of the dominating Laurentide Ice Sheet (LIS; Fig. 1), thereby contributed to the ice discharge[6,7]. The following extensive release of glacial freshwater disrupted interhemispheric ocean circulations, ultimately initiating an interglacial climate across the planet[6,8]. However, precisely dated ice-rafting events in the high latitude North Atlantic[9–11] indicate that the culmination of boreal iceberg discharge occurred thousands of years prior to the marked rise in air temperature recorded in the Greenland ice core[12] during the Last Termination (~20 to 8 ka BP[5,13,14]; Fig. 2a, b). Moreover, the initial reduction of Atlantic Meridional Overturning Circulation (AMOC) also preceded the episodic retreat of the LIS[9,15,16]. Numerical models suggest that ocean temperature warming can cause the retreat of the grounding lines and the melting of marine-based portions of the ice sheet, which may further

[1]College of Marine Geosciences, Ocean University of China, Qingdao, China. [2]Key Laboratory of Marine Geology and Metallogeny, First Institute of Oceanography, Ministry of Natural Resources, Qingdao, China. [3]State Key Laboratory of Tibetan Plateau Earth System, Resources and Environment (TPESRE), Institute of Tibetan Plateau Research, Chinese Academy of Sciences, Beijing, China. [4]Institute of Earth Science, University of Iceland, Reykjavik, Iceland. [5]Department of Marine and Coastal Science, Rutgers University, New Brunswick, NJ, USA. [6]Laboratory for Marine Geology, National Laboratory for Marine Science and Technology, Qingdao, China. [7]British Antarctic Survey, Cambridge, UK. ✉e-mail: yanguangliu@fio.org.cn; xuang@bas.ac.uk

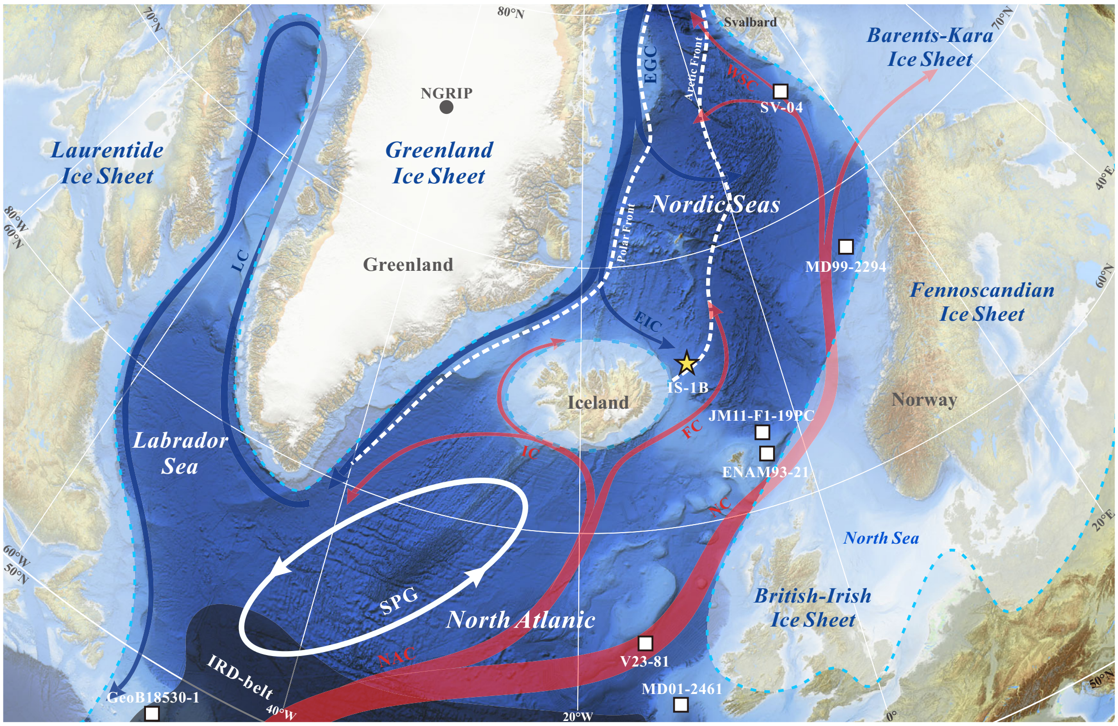

Fig. 1 | Location map of studied core and the pattern of modern surface ocean circulation in the study area. Yellow star: location of core site IS-1B (this study). White squares: location of reference core sites. Red arrows indicate modern warm inflow of Nordic Seas: NAC (North Atlantic Current), NC (Norwegian Current), FC (Faroe Current), IC (Inminger Current) and WSC (Western Spitsbergen Current); dark blue arrows indicate modern cold outflow of Nordic Seas and Labrador Sea: EGC (East Greenland Current), EIC (East Iceland Current) and LC (Labrador Sea Current); solid white line indicate SPG (Subpolar Gyre); white dashed line indicate Arctic Front and Polar Front[119,120]. The area shaded in white indicates the approximate extent of ice sheets during the LGM[25] and the area shaded in black indicates the ice-rafted detritus (IRD) belt in the North Atlantic[121]. Base map is redrawn from the EMODnet GeoViewer (https://emodnet.ec.europa.eu/geoviewer/), created by EMODnet (https://emodnet.ec.europa.eu/), and is owned by the EU and licensed under the Creative Commons Attribution 4.0 International (CC BY 4.0) license (https://creativecommons.org/licenses/by/4.0/deed.en).

destabilize the continental ice sheets[17,18]. This implies that, besides atmospheric warming, oceanic processes could have also served as a key trigger for the collapse of the Northern Hemisphere ice sheets[9,15], and the coupled ocean-ice sheet system may exhibit more prompt feedbacks to insolation changes and internal ice-sheet oscillations at the onset of the Last Termination[5,19,20]. To comprehend the mechanisms that triggered the Last Termination, it is crucial to determine the extent to which the decay of Northern Hemisphere ice sheets is linked to the environmental conditions of the surrounding oceans, and how such an indirect solar-driving mechanism can produce the sensitive oceanic response observed at the end of a glaciation cycle.

In high latitudes, the effects of insolation are considered to be potentially amplified in climatically sensitive ocean regions and efficiently transmitted to the margins of ice sheets through thermohaline circulation[21,22]. Furthermore, the contrast in solar heating between the tropics and poles, that is, the latitudinal insolation gradient (LIG), can regulate the poleward transport of oceanic heat and moisture by modulating the latitudinal temperature gradient (LTG) and mid-latitude wind fields, directly influencing the dynamics of ice sheets[23,24]. During the Last Glacial Maximum (LGM, ~26.5 to 19 ka BP[25]), the Eurasian Ice Sheet complex (EIS) attained a peak ice volume responsible for around 24 m of eustatic sea-level fall[26,27], forming an extensive ice–ocean interface with the Nordic Seas and the North Atlantic[28,29]. The southern and western margins of the EIS were adjacent to the warm Norwegian Current, the downstream of the North Atlantic Current (NAC), and an integral part of the upper branch of the AMOC, thereby exposing the EIS to the impact from temperature fluctuations carried by Atlantic Water (AW)[30]. Since the Nordic Seas are the main gateway of the iceberg trajectory associated with the EIS, and large marine-based sectors of the glacial EIS extended all the way to the continental shelf edge bordering the Nordic Seas[31,32], the sedimentary records of the Nordic Sea are ideal for studying the interaction between ocean dynamics and the ice sheet instabilities. In the present study, we combined multi-geochemical proxy data from the southern Nordic Seas to reconstruct the evolution of upper ocean hydrography at the beginning of the Last Termination. Mechanisms responsible for AW variability are discussed with the aid of transient climate simulation TraCE, to better understand the role of insolation-driven northward oceanic heat transport on the early instabilities of the EIS. Furthermore, we assessed the impacts of intermittent iceberg discharges from the EIS on the early slowdown of AMOC prior to Heinrich Stadial 1 (HS1, ~17.1 to 14.3 ka BP[33]) and on the destabilization of LIS.

Results and discussion

Geological setting, chronology, and geochemical proxies

During the 5th China Arctic Research Expedition in August 2012, a gravity core (ARC5-IS-1B, 65°36′N, 8°59′W, hereafter IS-1B) was retrieved in the north of the Iceland-Faroe Ridge at 819 m water depth (Fig. 1). The core site lies beneath the path of the modern Faroe Current, the main branch of the warm AW inflow and an integral component of the upper branch of the AMOC[34,35]. Instrumental and historical records indicate that the East Icelandic Current can also occasionally influence the surface water at this location, suggesting that IS-1B may serve as a sensitive archive for the past ocean dynamics in temperature and salinity[36–38]. The chronostratigraphic framework of core IS-1B is established by eight accelerator mass spectrometry radiocarbon (AMS ^{14}C) ages spanning the past ~30 ka. We measured the Mg/Ca ratio of dominantly polar water-dwelling planktonic foraminifera *Neogloboquadrina pachyderma* sinistral (*N. pachyderma* (s)) as a proxy for the

https://doi.org/10.1038/s41467-026-73152-7

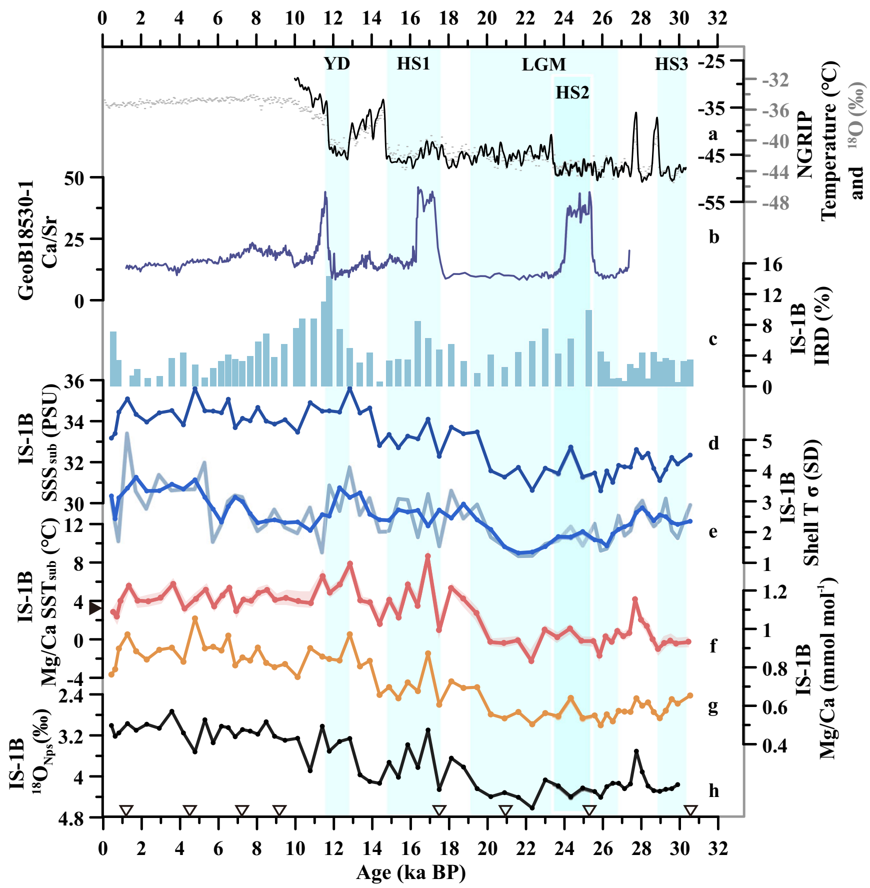

Fig. 2 | Downcore variation of multiple proxies in core IS-1B sediment in comparison to the NGRIP and North Atlantic proxy records over the last 30 ka. **a** North Greenland Ice Core Project (NGRIP) stable oxygen isotopic composition ($\delta^{18}O$) and temperature from ice core[121–124]. Grey dots indicate the $\delta^{18}O$ and the black line indicates the temperature. **b** Ca/Sr from core GeoB18530-1, reflecting detrital carbonate IRD layers[9]. The elevated Ca/Sr ratios are attributed to the high content of detrital carbonate IRD originating from Paleozoic limestone and dolostone in Hudson Bay and Hudson Strait[125]. **c** IRD (>125μm) content from core IS-1B. **d** Shallow subsurface water mass salinities (SSS_{sub}) calibrated from the $\delta^{18}O$ of the *N. pachyderma* (s) from core IS-1B. **e** Standard deviation of single shell Mg/Ca temperatures in each sampling layer of core IS-1B, the blue line is a 3-point running average of the gray line data. **f** Shallow subsurface water mass temperatures (SST_{sub}) calculated from the Mg/Ca of *N. pachyderma* (s) from core IS-1B; shaded envelopes represent the 95% confidence interval of the Mg/Ca-derived temperature reconstructions; the black triangle on the Y axis indicates the modern temperature (3.26°C, World Ocean Atlas 2023[106]) of core-top *N. pachyderma* (s) calcification depth. **g** Mg/Ca of *N. pachyderma* (s) from core IS-1B. **h** $\delta^{18}O$ values of *N. pachyderma* (s) from core IS-1B. The white triangles on the X axis indicate the calibrated radiocarbon age control points (AMS ^{14}C ages). The shaded blue bars denote cold stages: Younger Dryas (YD), Heinrich Stadial (HS), and Last Glacial Maximum (LGM).

temperature of shallow subsurface water mass (SST_{sub}; Supplementary Materials). The positive correlation between salinity and the stable oxygen isotopic composition of seawater ($\delta^{18}O_{sw}$) is widely accepted across different oceans[39–41], so that we calculated the ambient $\delta^{18}O_{sw}$ derived from *N. pachyderma* (s) to estimate the salinity of the shallow subsurface water mass (SSS_{sub}) after correcting for the global ice-volume effect. To further monitor the variability of shallow subsurface water mass and the stability of upper ocean structure in response to the fluctuations in northward heat flux, we reconstructed the Mg/Ca-derived temperatures from individual foraminiferal shells within each sampling layer, together with their standard deviation (Supplementary Materials), to investigate the magnitude of temperature fluctuations at the sampling-interval resolution (~180–720 years).

Upper ocean warming in the Nordic Seas since the late stage of LGM

In the Nordic Seas, the evolution and spatial extent of inflowing AW are closely linked to the sea-ice dynamics and meltwater input controlled by regional climate[42]. More recent reconstructions and modeling simulations have indicated that the warm AW never ceased to flow into the Nordic Seas during the glacial period, but rather subducted to the subsurface and intermediate layers below the halocline and sea ice[43–45]. Our new SST_{sub} records from core IS-1B show relatively low values over most of the LGM. However, an intriguing temperature increase of 5.62 ± 0.57 °C after 20.16 ka BP marks a distinct shift from the previous interval characterized by weak fluctuations near the freezing point, indicating the onset of shallow subsurface warming in the southern Nordic Seas during the late stage of the LGM (Fig. 2f). At the same time, the increase in SSS_{sub} reveals the occurrence of a saltier shallow subsurface layer and a weaker vertical salinity gradient relative to the underlying AW (Fig. 2d).

Another salient feature is the synchronous increase in the standard deviation of Mg/Ca temperatures derived from individual shells (Fig. 2e). This drastic increase in the temperature dispersion indicates that temperature within the shallow subsurface layer varied more frequently and across a wider range on centennial timescales. Combined with the growth of average temperature, the increased variability of individual shell temperature signals most probably indicates instability of the shallow subsurface layer. This instability and the warming trend could be further associated with a thinner and weakly stratified halocline caused by the regional shoaling of subducted warm AW, ultimately facilitating upward AW heat transfer and upper ocean warming, analogous to the ongoing Atlantification phenomenon observed in the modern Eurasian Basin[46,47].

https://doi.org/10.1038/s41467-026-73152-7

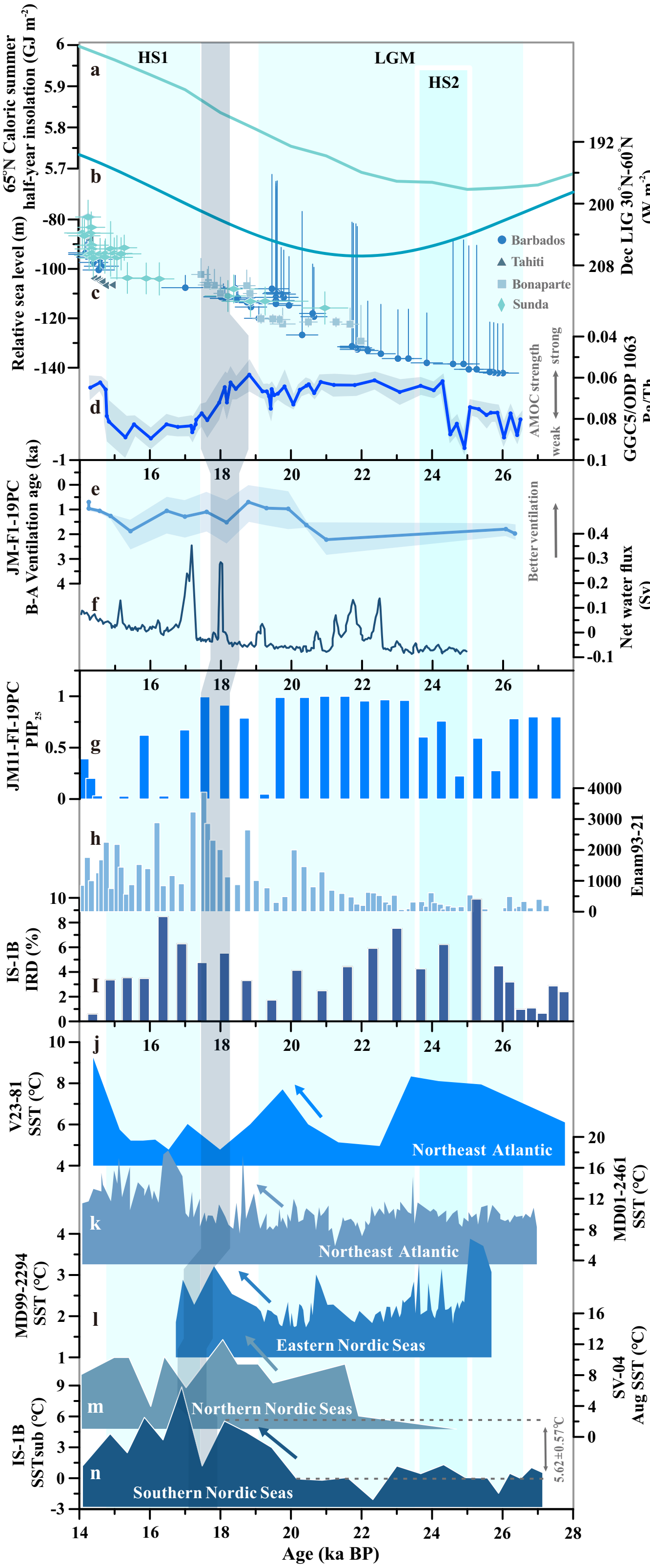

Fig. 3 | Comparison of proxy records between core IS-1B and representative cores in the North Atlantic and the Nordic Seas. **a** Caloric summer half-year insolation at 65°N[1] **b** Winter insolation gradient between 30-60°N[56]. **c** Relative sea level reconstructed from Barbados[126], Bonaparte Gulf[127,128], Tahiti[129,130] and Sunda Shelf[131]. **d** The Pa/Th ratio from the Bermuda Rise. Time series from 0 to 19 ka BP derived from the core GGC56[83] and the time series from 20 to 27 ka BP derived from core ODP1063[84]; shaded envelopes indicate the analytical uncertainty (2σ) of the Pa/Th. **e** Benthic foraminifera-atmosphere ^{14}C age offsets from core JM-F1-19PC[52]; shaded envelopes indicate the propagated uncertainty derived from uncertainties in foraminiferal ^{14}C measurements, the atmospheric ^{14}C records, and the age model. **f** Time series of simulated global freshwater input[73]. **g** P_BIP_{25} signals of sediment core JM11-FI-19PC[55]. **h** IRD (lithics >150 μm) counts from core Enam93-21[132]. **i** IRD (>125 μm) contents from core IS-1B (this study). **j** Surface temperatures calculated by foraminiferal transfer functions from core V23-81[49]. **k** Mg/Ca-based surface sea temperatures measured on *G. bulloides* from core MD01-2461[48]. **l** Surface temperatures calculated by foraminiferal transfer functions from core MD99-2294[50]. **m** August surface sea temperatures derived from dinocyst assemblages from core SV-04[51]. **n** Shallow subsurface water mass temperatures (SST_{sub}) calculated from the Mg/Ca of *N. pachyderma* (s) in this study; the warming trend since 20.16 ka BP is statistically significant at the 95% level (using Student's t test). The shaded blue bars indicate the cold stages, and the shaded black bar indicates the cooling phase identified in the Nordic Seas and the North Atlantic.

Further comparisons of proxy records from adjacent stations in the Nordic Seas and North Atlantic, alongside the results of TraCE simulations, yield two key observations. First, the general trend of temperature increase since the late LGM is also visible in surface North Atlantic along the path of NAC[48,49], in the eastern Nordic Seas margin stations close to the Fennoscandian Ice Sheet[50] (FIS) and Barents-Kara ice sheets[51] (BKIS), as well as in the temperature profiles simulated by the TraCE model (Fig. 3j, k, l, m and Fig. 4a). This warming trend is not so pronounced and shorter in duration compared to other amplitudes observed in the Bølling-Allerød period and Holocene. Nonetheless, the presence of similar upper ocean warming signals farther downstream along the AW pathway[51] (Fig. 3m) reveals that the northern boundary of this transient warming may have reached the Svalbard Islands, potentially influencing the entire Nordic Seas from south to north.

Secondly, evidence of prominent warm intermediate water appears in the benthic records from the southeastern Nordic Seas, suggesting a continuous inflow of AW throughout most of the LGM[43]. The correlation with the consistent surface warming in the subpolar North Atlantic likely reflects substantial ocean heat accumulation during the late stage of LGM[48,49] (Figs. 3j, k, 4a), which in turn accelerated the northward heat transport and facilitated the development of a subsurface heat reservoir in the Nordic Seas. Although the large benthic-atmosphere ^{14}C age offset indicates that the Faroe–Shetland Channel (the southern Nordic Seas) was poorly ventilated during much of the LGM[52], a subsequent reversed decrease in ventilation age can presumably be considered as a phased resumption of upper ocean convection beginning around 20.44 ka BP (Fig. 3e). Similar to the constantly strengthening Atlantification process in the modern Eurasian Basin, the shoaling of AW likely weakened the surface stratification and the halocline, further promoting progressively winter ventilation and heat redistributions in the upper ocean[46,53]. The onset of SST_{sub} increase observed in our records, coinciding with the enhanced ventilation in the southern Norwegian Sea[52] (Fig. 3e, n), provides supporting evidence for a similar mechanism during the late stage of the LGM, in which the AW shoaling played a causal role in strengthening the surface-deep mixing and driving the upper ocean warming. In particular, the substantial heat delivery from AW could have influenced sea-ice dynamics and caused a further retreat of the ice margins in the late-glacial Nordic Seas[54]. Consistently, PIP_{25} records from the southern Norwegian Sea also indicate that a perennial ice-free condition may have prevailed during this stage[55] (Fig. 3g). Thus, the potential contribution of the continuous heat transport from AW and this millennial-scale warming trend to the altered climate should not be ignored.

High-latitude oceanic response to the insolation changes

From a broader perspective, the observed changes in surface and subsurface Nordic Seas hydrography during the late stage of LGM could have been a regional feedback mechanism to global-scale climate driving forces. Our reconstructed temperature standard

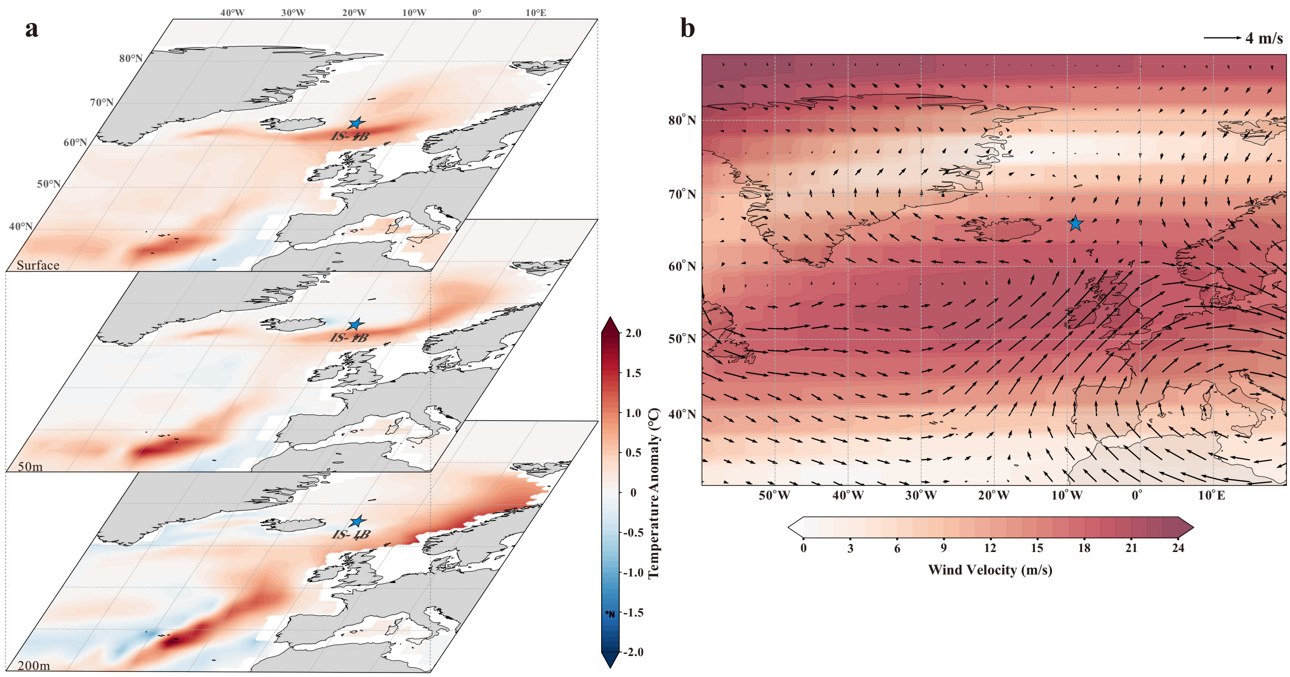

Fig. 4 | TraCE simulated oceanic and atmospheric changes in the North Atlantic and the Nordic Seas. a Annual ocean temperature anomalies (19-21 ka BP) along the upper ocean (surface, 50 m and 200 m depths) of the Atlantic and the Nordic Seas, simulated under all forcings. The blue star marks the core IS-1B location. **b** Winter anomalies (19–21 ka BP) of 850 hPa wind (vectors) and surface wind (shaded color) over the North Atlantic and Nordic Seas, simulated under isolated insolation forcing. The blue star marks the core IS-1B location.

deviations (Fig. 2e) indicate that the onset of instability in shallow subsurface water mass and upper halocline layer, likely resulting from enhanced shoaling of AW, could have occurred as early as ~21 ka BP. Notably, the timing of initial AW shoaling is concurrent with the significant recovery of 65°N caloric summer half-year insolation[56,57] (Fig. 3a), which may imply a close linkage between solar forcing and heat accumulation in the AW layer of the Nordic Seas. Furthermore, the concurrent weakening of winter LIG between 60°N and 30°N[24,56], together with the subsequent basin-wide warming trend (Fig. 4a), indicates that the latitudinal variations in external insolation forcing may have been accompanied by positive regional oceanic feedback processes.

Under glacial conditions, the apparent immediate oceanic response to the growing boreal insolation in the Nordic Seas can be shown in the reduced sea ice cover and lower ice-albedo feedback, as well as the in situ surface water warming affecting the hydrographic conditions[58–60]. However, several model simulations reveal that the energy of local insolation is insufficient to drive large-scale surface warming associated with the ice sheet instabilities and major climate transitions in the Northern Hemisphere[5,25,61,62]. The linkages between oceanic feedbacks in the Nordic Seas and solar forcing are most likely tied to the orbitally forced modulations of atmospheric-oceanic variability and the poleward flux of latent/sensible heat transported by AW. Indeed, the solar influence on climate of the magnitude and consistency implied by our evidence could not only have been confined to the Nordic Seas.

It has been proposed that the LIG can influence the Northern Hemisphere climate system by modulating the LTG, which in turn affects the mid-latitude storm tracks, as well as the position of subtropical high- and subpolar low- pressure centers[63–65]. As demonstrated in the late Pleistocene and Holocene, increased boreal insolation can lead to a reduced winter LIG and a weakened LTG, which have been found to cause poleward shifts of the westerly flow[23,24]. These changes in atmospheric circulation modified the wind stress across the North Atlantic and further promoted the transport of warm AW into the Nordic Seas[23,24]. Similarly, results from the TraCE simulations[8,66] indicate that isolated orbital forcing can lead to an increase in the intensity of 850 hPa wind south of Iceland since 21 ka BP (Fig. 4b; Supplementary Materials), which is also consistent with the trend toward a northward-intensified westerly flow. This strengthened wind stress in the cyclone direction can present a pronounced east-west extension of subpolar gyre[67,68] (SPG), resulting in a stronger NAC with enhanced northward heat transport into the North-East Atlantic and the Norwegian Seas[68–70]. Meanwhile, the TraCE results reveal that the increasing insolation also strengthened the winter surface winds in the Nordic Seas since the late stage of the LGM[8,66] (Fig. 4b), implying that the enhanced surface winds may have further intensified the vertical mixing and facilitated the shoaling of the subsurface AW[71]. We thus infer that the observed upper-ocean warming in the Nordic Seas and the intensified Atlantification-like process were primarily driven by coupled atmospheric–oceanic circulation changes that were initiated by orbitally forced reductions in the LIG.

A pivotal role of upper ocean processes in triggering EIS termination and deglacial climate

The reduction of the LIS and EIS from maximum volume and the acceleration occurring during HS1 represent a rapid transition in recurring ice sheet cycles and the termination of last glaciation climate[5,22,72]. At the onset of the deglaciation stage, a period of cold shallow subsurface conditions since around 18.11 ka BP, following the anomalous warming event in the late LGM, is captured by our *N. pachyderma* (s) Mg/Ca-derived temperature and the enhanced IRD concentrations observed at the sites in the southern Norwegian Sea (Fig. 3h, i, n). This is in line with the substantial meltwater release recognized in the margins of the EIS during the same interval and is further supported by recent transient climate model estimates, which identified the first deglacial meltwater peak at ~18 ka BP[73–76] (Fig. 3f). Paleoglaciological studies document a significant ice margin retreat of the British-Irish Ice Sheet (BIIS) and FIS accompanied by the disintegration of the North Sea Ice Bridge at ~18 ka BP, which resulted in the

https://doi.org/10.1038/s41467-026-73152-7

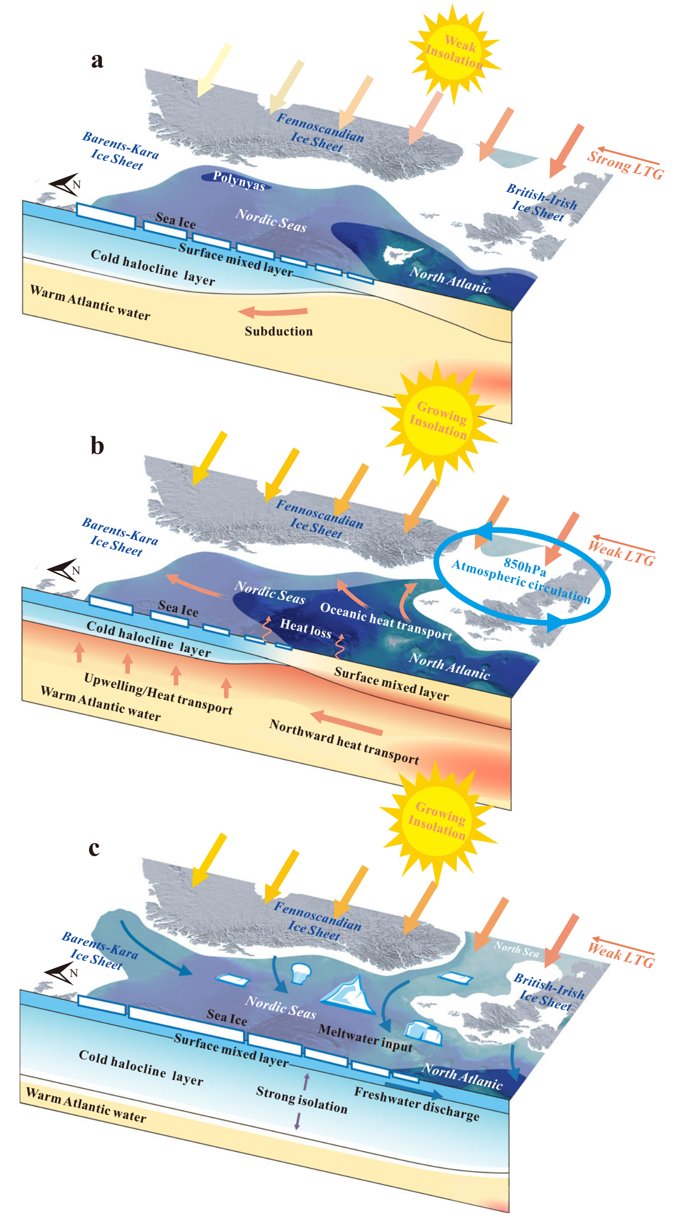

Fig. 5 | Cartoon of upper ocean water masses evolution of Nordic Seas. a Early LGM. Weak boreal insolation and strong LIG; expanding EIS; extensive sea ice and strengthened stratification; warm AW subducted beneath the cold halocline and the surface mixed layer. **b 19 ka BP.** Significantly increased insolation and weakening LIG; stronger 850 hPa wind in cyclonic direction; intensified northward heat transport; AW shoaled, thinned halocline and strengthened oceanic heat release. **c 18 ka BP.** Large-scale EIS collapse; freshwater discharge into North Atlantic via the Nordic Seas; thickened halocline; AW retreated to subsurface/intermediate depths. Base map is redrawn from the EMODnet GeoViewer (https://emodnet.ec.europa.eu/geoviewer/), created by EMODnet (https://emodnet.ec.europa.eu/), and is owned by the EU and licensed under the CC BY 4.0 license (https://creativecommons.org/licenses/by/4.0/deed.en).

collapse of an ice-dammed lake in the North Sea and triggered an enormous meltwater outburst into the Nordic Sea and North Atlantic[74,75,77,78]. At the same time, the rapid withdrawal of the grounding line of the Bjørnøyrenna Ice Stream, which lay beneath and drained the southwestern sector of BKIS, has also led to sustained freshwater discharge, likely contributing to the surface cooling and the elevated IRD flux in Nordic Seas during this interval[79,80].

At its maximum extension during the LGM, the EIS expanded to include a large marine-based sector that was exposed to oceanic variations, particularly in the BKIS and the northern BIIS[27]. In addition, sea level changes and oceanic processes also strongly influenced the stability of the marine-based ice shelves during stadial-interstadial transitions[17,30,81]. Modeling studies showed that basal melting, induced by oceanic temperature fluctuations, may be more efficient than surface mass balance changes in leading the higher rates of iceberg discharge along the EIS margins and the meltwater peaks on the multi-millennial evolution[30,80]. Rørvik et al. argued that the main IRD maxima and plumate deposition records in the Norwegian shelf post-date periods with increased adjacent sea temperature, indicating that upper ocean warming was probably a key external forcing on the fast-flowing paleo-ice streams and enhanced meltwater release from the FIS during the late LGM and early deglaciation[50,78]. Building on the observed correspondence between the anomalously warm conditions and meltwater activities recorded in our study region and along margins of the FIS[50,78], the BIIS[48] and the BKIS[80], we presume that the extensive upper ocean warming in the Nordic Seas and the strengthened ocean heat transport to the grounding line promoted sustained melting of the marine-terminating glaciers and led to a progressive weakening of ice-shelf buttressing. This may have triggered the rapid collapse of the EIS, leading to massive iceberg/meltwater output at the beginning of the Last Termination (Fig. 5b). While many studies have emphasized the significant role of atmospheric warming in driving EIS instability[82], its relative contribution remains debated in current ice-sheet model simulations[30,31,80]. We also acknowledge the potential influence of atmospheric warming in this study. However, considering the mechanistic framework of EIS dynamics and the relatively modest magnitude of reconstructed surface air temperature warming during this interval[31,80,82,83], we propose that, much like sea-level rise, atmospheric warming may have primarily acted to amplify the sensitivity of the EIS to oceanic temperature fluctuations and associated basal melting.

Evidence from the benthic-atmosphere ^{14}C age offset reconstruction at 18.16 ka BP suggests that the enhanced freshwater flux may have hampered the Nordic Seas surface convection and deep-water ventilation[52] (Fig. 3e). At this point, the proxy records of Pa/Th show an early decline of AMOC strength[84,85] (Fig. 3d), which reflects the initial reduction of ocean circulation in the high latitude Atlantic prior to HS1. Multiple lines of proxy and modeling evidence suggest that meltwater from European sources, rather than from North America, associated with instability of the LIS, had already intruded into the mid-latitude Atlantic preceding the HS1, and may have contributed to the shutdown of North Atlantic Deep Water (NADW) formation[9,73]. This interpretation is further supported by the presence of additional European-origin IRD fluxes that predate the LIS surges within the North Atlantic Heinrich layer[86,87]. Based on this, we hypothesize that the meltwater pulse responsible for the initial slowdown of AMOC prior to HS1 primarily originated from the contemporaneous rapid melting of EIS.

Physically, meltwater discharged through the Nordic Seas would have led to a direct isolation of AW and the formation of a stronger halocline, ultimately resulting in the redistribution of heat in the upper layer and a basin-wide subsurface warming in the Atlantic[9,15,44,88](Fig. 5c). Several model simulations have indicated that AMOC reduction configures a feedback mechanism with subsurface ocean warming, which even can extent to depths of approximately 2,500 m due to the continued downward mixing of heat in the Atlantic basin[15,45]. This subsurface temperature anomaly can propagate on advective timescales (within a few decades) toward the Labrador Sea[15]. Enhanced heat transfer would accelerate the basal melting below the Labrador ice shelf, substantially increasing the calving rate of the LIS[15,88]. Accordingly, the sudden loss of buttressing is considered to have resulted in substantial ice shelf disintegration of LIS corresponding to the first pronounced peak of IRD flux and freshwater discharge, marking the prologue of HS1 and deglaciation climate[17].

Beyond these ocean–ice sheet interactions, variations in the global carbon cycle are also considered to have played a critical role in shaping the termination process[4,5,89]. However, Cheng et al.[4] proposed that in the last four terminations, the initial disintegration of northern ice sheets slowed down the Meridional Overturning Circulation, which then, through the bipolar seesaw mechanism, drove a warmer Southern Ocean and the subsequent enhancement of CO_2 ventilation as feedbacks. Meanwhile, the apparent rise in atmospheric CO_2 concentrations recorded in ice cores also lagged behind the warming trend in the Nordic Sea and the initial collapse of the EIS[90,91]. Therefore, we are more inclined to regard the increase in atmospheric CO_2 as a key factor in completing the terminations rather than triggering them.

Overall, both solar insolation, thermal transformation, and ocean-ice sheet interactions were clearly interlocked in the millennia preceding HS1. This explains why it is critical to highlight the role of upper ocean activities in the initiation of the Last Termination. We propose that the anomalous upper ocean warming in the Nordic Seas amplified the effect of boreal summer insolation and LIG, contributing to the meltwater surge from the EIS at the beginning of the Last Termination. This signifies an early and prompt feedback of the ocean heat conveyor system to insolation in initiating the collapse of Northern Hemisphere ice sheets. Subsequently, the enhanced freshwater release through the Nordic Seas shifted the North Atlantic into a state with weak AMOC and NADW formation, further inducing large-scale subsurface warming and triggering the destabilization of the LIS[9,15]. Our findings expand the climatological evolutionary chain of the driving mechanisms for the initial collapse of Northern Hemisphere ice sheets to an earlier period (the late stage of the LGM), and support the view that the sensitive oceanic responses to insolation changes served as a key trigger of the climate transition in the Last Termination.

Methods

Age models

Radiocarbon (^{14}C) analyses were performed at the Beta Analytic Laboratory, Florida, USA, on the dominant foraminifera *N. pachyderma* (s), using accelerator mass spectrometry (AMS) to establish the chronostratigraphic framework. We picked *N. pachyderma* (s) up to a weight of ~12 mg within the 250–350 µm size fraction from eight representative layers for AMS measurement.

To establish the calendar age-depth model, radiocarbon dates were calibrated using the Bayesian age-modeling approach implemented in the R package Bacon, employing the Marine20 calibration curve[92,93]. Uncertainties in reservoir age corrections when applying the Marine20 curve are particularly pronounced in high-latitude polar regions, due to variations in sea ice extent and ocean ventilation during glacial periods[93]. To account for this, we applied a Holocene reservoir correction (ΔR_{Hol}) to estimate the upper bound of calendar ages, and a glacial reservoir correction (ΔR_{GS} and ΔR_{CS})-derived from modeled latitudinal reservoir age estimates-to establish the lower age bound following the method of Heaton et al.[94]. The Holocene ΔR_{Hol} value was set to −86 ± 65 years, calculated based on 10 modern ΔR values from stations located within 500 km around the core IS-1B site (http://calib.org/marine/). For the glacial period (pre-Holocene), an additional ΔR offset was added to the original Holocene ΔR_{Hol} to account for the latitudinal increases in the reservoir ages. Accordingly, the local maximum ΔR correction for the cold stadial scenario (HS1) was estimated as ΔR_{CS} = ΔR_{Hol} + 1320 = 1234 ± 65 years, and for the full glacial scenario as ΔR_{GS} = ΔR_{Hol} + 1370 = 1284 ± 65 years (ΔR offsets derived from 66.25°N data, near the core IS-1B site[94]). A single age-depth model was then developed by averaging the mean ages from both the Holocene and glacial corrected age-depth models to constrain the final age estimates[95] (Fig. 6; Supplementary Materials).

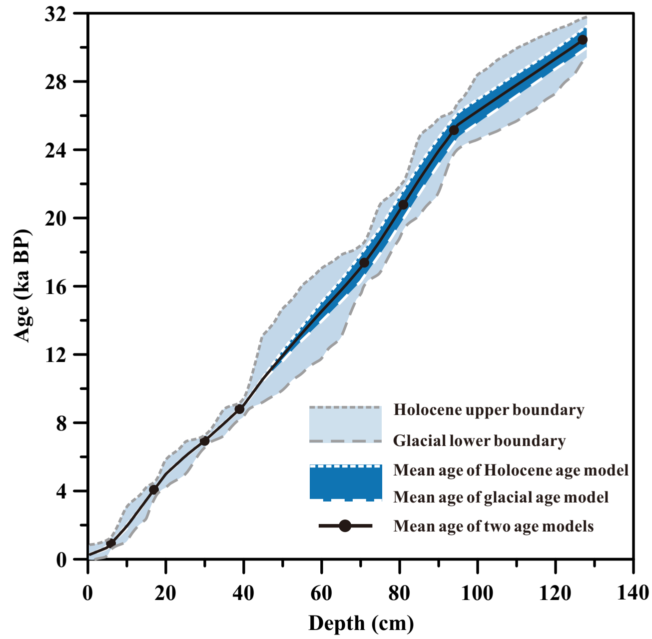

Fig. 6 | Age-depth models of core IS-1B. The white dashed lines represent the age-depth models developed individually by Bacon using two different reservoir age corrections, the Holocene and glacial corrections, respectively. The light blue shading denotes the combined 95% confidence interval of both age-depth models. The solid black line indicates the mean of these two age-depth models and is adopted as the final age-depth model used in this study.

Oxygen isotope

Stable oxygen isotope analysis of planktonic foraminifera ($\delta^{18}O_c$) was carried out on 20–25 specimens of *N. pachyderma* (s) using a mass spectrometer (Finnigan MAT 252) combined with the carbonate preparation device (Kiel III) at the Light Stable Isotope Mass Spectrometry Laboratory, Department of Geological Sciences, University of Florida. Data are reported in per-mil notation (‰) relative to the Vienna Pee Dee Belemnite (VPDB) scale and referenced to the NBS18 standard ($\delta^{18}O_{VPDB}$ = − 23.0 ± 0.1‰). The analytical standard deviation indicated by replicate measurements was less than 0.07‰.

Mg/Ca temperatures of *N. pachyderma* (s) and salinity of shallow subsurface water mass

For the Mg/Ca ratio measurements, 12 specimens of *N. pachyderma* (s) (intact, no contamination, ~300 µm size fraction) were picked from each layer of the sediment core at 2 cm intervals. The foraminiferal samples were first ultrasonically washed in deionized water and methanol to remove clay, followed by oxidative cleaning by immersion in hydrogen peroxide to remove organic material[96]. The Mg/Ca ratios were measured using a Thermo Scientific RQ ICP-MS coupled to a Geolas ArF excimer laser at the Key Laboratory of Marine Geology and Metallogeny at the First Institute of Oceanography, Qingdao, China. An N_2 gas stream was used to transport the ablation products to the RQ ICP-MS.

The RQ ICP-MS instrument response was calibrated using SRM NIST610, 612, and 614 glasses and corrected for variations in the ablation yield and instrument drift by normalizing to the measured internal standard elements (^{88}Sr and ^{55}Mn) intensities during each mass spectrometer cycle[97,98]. To isolate only the banding patterns in our data, ICPMSDataCal12.2[99,100] software was applied to the RQ ICP-MS signals to remove low- and high-frequency noise. Abnormal signal peaks of Mg, Fe and Mn during the initial 3–5 s of ablation reflect contamination in the outermost shell layer caused by post-depositional diagenesis (Fig. 7). We therefore ignored these high signal zones and used the subsequent 15–30 s of continuous and stable

 https://doi.org/10.1038/s41467-026-73152-7

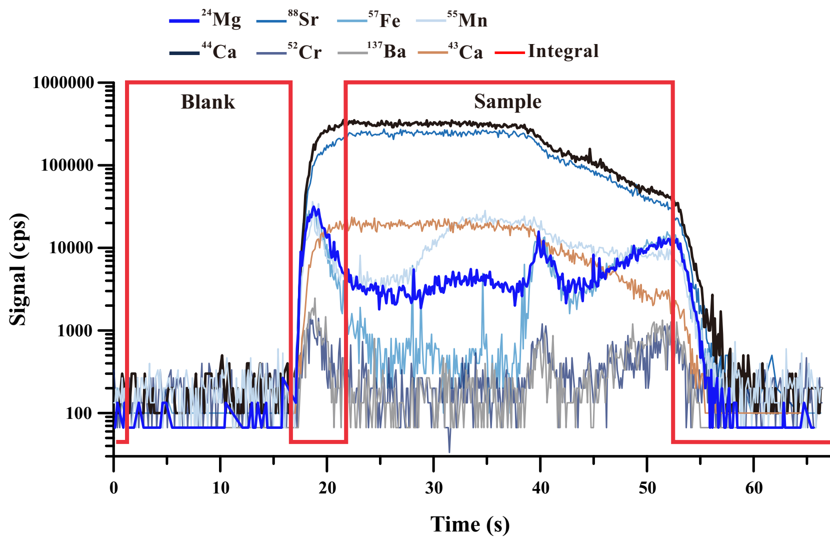

Fig. 7 | Typical profile of LA-ICP-MS signals. Profiles are displayed from the outer to the inner surface of the shell wall. The thick red line delineates the background signal and the selected valid signal interval. Other lines indicate signals of the corresponding elements (labeled on the top): ^{24}Mg, ^{88}Sr, ^{57}Fe, ^{55}Mn, ^{44}Ca, ^{52}Cr, ^{137}Ba, ^{43}Ca.

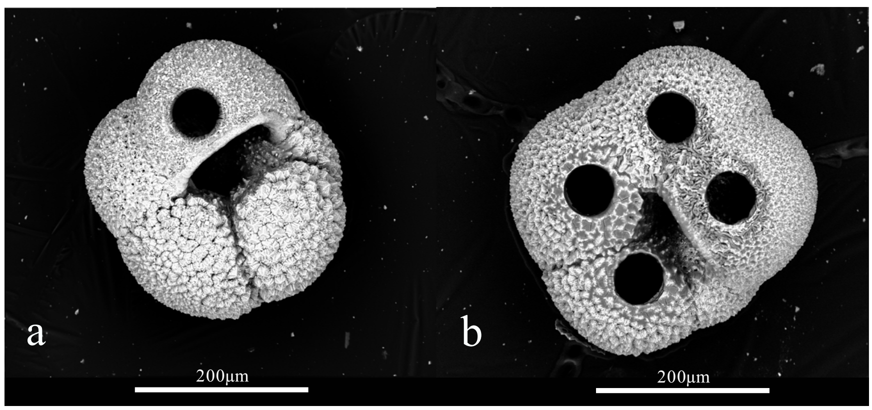

Fig. 8 | Scanning electron microscope image of laser-ablated *N. pachyderma* (s) shells. a Ablation test on the final chamber. **b** Comparison ablation test on different chambers.

signals, encompassing both the crust and the inner ontogenetic calcite, to obtain a more stable and accurate reconstruction of the elemental ratios. Mg/Ca ratios for each sample of *N. pachyderma* (s) were determined based on the ratios of the average polished signal intensities along the ablation profile[101]. For each sediment layer, the Mg/Ca ratio was calculated as the average of 12 individual shell measurements.

Foraminiferal Mg/Ca ratios were converted into seawater temperatures, with particular consideration given to the influence of carbonate ion concentration in the low-temperature waters of subpolar regions[102–105]. To isolate the impact of carbonate ion on the Mg/Ca-derived temperatures, a Mg/Ca-[CO^{2-}_3] sensitivities correction was applied, which was established based on shell $\delta^{18}O_c$ and glacial-interglacial sea-level variations, following the approach of Morley et al.[104] (Supplementary Materials). Subsequently, shallow subsurface water mass temperatures (SST_{sub}) were estimated from the corrected Mg/Ca ratios ($Mg/Ca_{[Corr]}$) using the following equation:

$$Mg/Ca_{[Corr]} = 0.372 \pm 0.014\ \exp^{(0.0936 \pm 0.0045T)} \quad (1)$$

Comparison of converted Mg/Ca temperature from IS-1B core-top to modern instrumental temperatures allowed to evaluate the accuracy of temperature reconstruction. The reconstructed calcification depth of 50 m for modern *N. pachyderma* (s) at our core site yields a difference of 0.22 °C after calibration to Eq. 1, indicating a reasonably good agreement and supporting its suitability for reconstructing temperatures from the downcore samples[106] (Supplementary Materials).

The ambient seawater oxygen isotope ($\delta^{18}O_{sw}$) was calculated from SST_{sub} and foraminifera shells $\delta^{18}O_c$ using the equation of Shackleton[107] and O'Neil et al.[108]. (Eq. 2) with calibration to convert the calcite value from the VPDB to the Vienna Standard Mean Ocean Water scale[109] ($\delta^{18}O_{sw,\ V\text{-}SMOW}$, Eq. 3).

$$\delta^{18}O_{sw} = \delta^{18}O_c - (4.38 - \sqrt{4.38^2\text{-}0.4(16.9\text{-}T)})/0.2 \quad (2)$$

$$\delta^{18}O_{sw,\,V-SMOW} = (\delta^{18}O_{sw} + 0.2‰)/0.998 \quad (3)$$

The oxygen isotopic composition with the global ice-volume and sea-level effects removed ($\delta^{18}O_{sw\text{-}local}$), and the salinity in the shallow subsurface water mass (SSS_{sub}) were reconstructed using Eq. 4[110,111] and Eq. 5[109].

$$\delta^{18}O_{sw-local} = \delta^{18}O_{sw,\,V-SMOW} - 0.0083‰ \times SL \quad (4)$$

$$SSS_{sub} = (\delta^{18}O_{sw-local} + 12.17 \pm 1.18)/0.36 \pm 0.03 \quad (5)$$

Where SL is sea level changes come from the curve of Lambeck et al.[26].

LA-ICP-MS test conducted on *N. pachyderma* (s)

There was a significant difference in the shell diameter and thickness of *N. pachyderma* (s) in different sea areas. Therefore, we tried different laser intensities, pulse rates, and ablation scopes to obtain steady and clear signals of *N. pachyderma* (s) in core IS-1B. Experiments ultimately showed that the 60 μm diameter circular spots and laser pulse rate of 4 Hz at a fluence of 3 J/cm^2 coupled well with *N. pachyderma* (s), yielding consistent signals lasting 15–30 s.

Considering the growth cycle of different chambers in *N. pachyderma* (s), we performed laser ablation on the four largest chambers in a single shell to compare the Mg/Ca between chambers (Fig. 8b). Results from different sediment layers show that the Mg/Ca temperature differences among the four chambers within a single *N. pachyderma* (s) shell are less than 0.47 °C. This variation is much smaller than both the temperature amplitudes observed in our time series and the summer–winter temperature difference of the ambient water[106]. We conclude that the effects of ontogenetic difference and growth cycle on the Mg/Ca ratios among different chambers of *N. pachyderma* (s) are minor in our core site, consistent with the results from laboratory culture experiments[112,113]. Therefore, the final chamber with a bulky and thick shell wall was selected for ablation (Fig. 8a). The laser ablation process in all tests was stable and continuous, proceeding from the outer surface to the inner part through the entire shell of *N. pachyderma* (s).

TraCE Experiments

We employed the TraCE simulation results[8,66] to assess remote North Atlantic forcing in response to changes of insolation. The TraCE transient climate experiments were performed in the Community Climate System Model ver. 3[114–116] (CCSM3), a global coupled atmosphere-ocean-sea ice-land general circulation model (AOGCM) that has a latitude–longitude resolution of ~3.75° in the atmosphere and ~3° in the ocean and includes a dynamic global vegetation module. The prescribed forcings and boundary conditions for the full-forcing simulation included orbitally forced insolation changes, increasing atmospheric concentrations of the long-lived greenhouse gases, and retreating ice sheets and associated meltwater release to the oceans[8,66]. The transient sensitivity experiments adopted a factorized forcing scheme to allow isolating each of these forcings separately[117]. The isolated insolation forcing experiments were selected to simulate the changes in winter 850 hPa wind velocity and surface wind velocity from the onset of AW shoaling to the warming peak (19 ka BP anomalies relative to 21 ka BP), aiming to examine the effects of increasing boreal insolation on atmospheric circulation over the North Atlantic. We also compared the sea temperature anomalies between 19 and 21 ka BP in the all-forcing simulation to examine the oceanic process related to this warming trend. All the changes were analyzed with Student's *t*-test, with confidence levels greater than 95%.

Data availability

All measurement data of core IS-1B used in this study are available at Figshare Data Repository (https://doi.org/10.6084/m9.figshare.30536837)[118]. All model output and scripts of TraCE transient climate experiments used in this study are archived at https://doi.org/10.5065/CXB5-TV56.

References

1. Berger, A. & Loutre, M. F. Insolation values for the climate of the last 10 million years. *Quat. Sci. Rev.* **10**, 297–317 (1991).
2. Hays, J. D., Imbrie, J. & Shackleton, N. J. Variations in the Earth's Orbit: Pacemaker of the Ice Ages. *Science* **194**, 1121–1132 (1976).
3. Ridgwell, A. J., Watson, A. J. & Raymo, M. E. Is the spectral signature of the 100 kyr glacial cycle consistent with a Milankovitch origin? *Paleoceanography* **14**, 437–440 (1999).
4. Cheng, H. et al. Ice age terminations. *Science* **326**, 248–252 (2009).
5. Denton, G. H. et al. The last glacial termination. *Science* **328**, 1652–1656 (2010).
6. Bintanja, R. & van de Wal, R. S. W. North American ice-sheet dynamics and the onset of 100,000-year glacial cycles. *Nature* **454**, 869–872 (2008).
7. Abe-Ouchi, A. et al. Insolation-driven 100,000-year glacial cycles and hysteresis of ice-sheet volume. *Nature* **500**, 190–193 (2013).
8. Liu, Z. et al. Transient simulation of last deglaciation with a new mechanism for Bølling-Allerød Warming. *Science* **325**, 310–314 (2009).
9. Max, L., Nürnberg, D., Chiessi, C. M., Lenz, M. M. & Mulitza, S. Subsurface ocean warming preceded Heinrich Events. *Nat. Commun.* **13**, 4217 (2022).
10. Barker, S. et al. Icebergs not the trigger for North Atlantic cold events. *Nature* **520**, 333–336 (2015).
11. McManus, J. F., Oppo, D. W. & Cullen, J. L. A 0.5-million-year record of millennial-scale climate variability in the North Atlantic. *Science* **283**, 971–975 (1999).
12. Buizert, C. et al. Greenland temperature response to climate forcing during the last deglaciation. *Science* **345**, 1177–1180 (2014).
13. Broecker, W. S. & van Donk, J. Insolation changes, ice volumes, and the O 18 record in deep-sea cores. *Rev. Geophys* **8**, 169–198 (1970).
14. Lisiecki, L. E. & Raymo, M. E. A Pliocene-Pleistocene stack of 57 globally distributed benthic δ 18 O records. *Paleoceanography* **20**, 1–17 (2005).
15. Álvarez-Solas, J. et al. Heinrich event 1: an example of dynamical ice-sheet reaction to oceanic changes. *Climate* **7**, 1297–1306 (2011).
16. Hall, I. R. et al. Accelerated drawdown of meridional overturning in the late-glacial Atlantic triggered by transient pre-H event freshwater perturbation. *Geophys. Res. Lett.* **33**, 1–5 (2006).
17. Alvarez-Solas, J. et al. Links between ocean temperature and iceberg discharge during Heinrich events. *Nat. Geosci.* **3**, 122–126 (2010).
18. Shaffer, G., Olsen, S. M. & Bjerrum, C. J. Ocean subsurface warming as a mechanism for coupling Dansgaard-Oeschger climate cycles and ice-rafting events. *Geophys. Res. Lett.* **31**, 1–4 (2004).
19. Fogwill, C. J. et al. Antarctic ice sheet discharge driven by atmosphere-ocean feedbacks at the Last Glacial Termination. *Sci. Rep.* **7**, 39979 (2017).
20. Huybers, P. & Wunsch, C. Obliquity pacing of the late Pleistocene glacial terminations. *Nature* **434**, 491–494 (2005).
21. Imbrie, J., McIntyre, A. & Mix, A. Oceanic Response to Orbital Forcing in the Late Quaternary: Observational and Experimental Strategies. in *Climate and Geo-Sciences* 121–164 Springer Netherlands, Dordrecht https://doi.org/10.1007/978-94-009-2446-8_7 (1989).
22. Palacios, D., Hughes, P. D., Sánchez-Goñi, M. F., García-Ruiz, J. M. & Andrés, N. The terminations of the glacial cycles. in *European Glacial Landscapes* 11–24 Elsevier, https://doi.org/10.1016/B978-0-323-91899-2.00002-4 (2023).
23. Davis, B. A. S. & Brewer, S. A unified approach to orbital, solar, and lunar forcing based on the Earth's latitudinal insolation/temperature gradient. *Quat. Sci. Rev.* **30**, 1861–1874 (2011).
24. Davis, B. A. S. & Brewer, S. Orbital forcing and role of the latitudinal insolation/temperature gradient. *Clim. Dyn.* **32**, 143–165 (2009).

25. Clark, P. U. et al. The Last Glacial Maximum. *Science* **325**, 710–714 (2009).
26. Lambeck, K., Rouby, H., Purcell, A., Sun, Y. & Sambridge, M. Sea level and global ice volumes from the Last Glacial Maximum to the Holocene. *Proc. Natl. Acad. Sci.* **111**, 15296–15303 (2014).
27. Hughes, A. L. C., Gyllencreutz, R., Lohne, ØS., Mangerud, J. & Svendsen, J. I. The last Eurasian ice sheets – a chronological database and time-slice reconstruction, DATED-1. *Boreas* **45**, 1–45 (2016).
28. Patton, H., Hubbard, A., Andreassen, K., Winsborrow, M. & Stroeven, A. P. The build-up, configuration, and dynamical sensitivity of the Eurasian ice-sheet complex to Late Weichselian climatic and oceanic forcing. *Quat. Sci. Rev.* **153**, 97–121 (2016).
29. Brendryen, J., Haflidason, H., Yokoyama, Y., Haaga, K. A. & Hannisdal, B. Eurasian Ice Sheet collapse was a major source of Meltwater Pulse 1 A 14,600 years ago. *Nat. Geosci.* **13**, 363–368 (2020).
30. Alvarez-Solas, J., Banderas, R., Robinson, A. & Montoya, M. Ocean-driven millennial-scale variability of the Eurasian ice sheet during the last glacial period simulated with a hybrid ice-sheet–shelf model. *Climate* **15**, 957–979 (2019).
31. Sejrup, H. P. et al. The role of ocean and atmospheric dynamics in the marine-based collapse of the last Eurasian Ice Sheet. *Commun. Earth Environ.* **3**, 119 (2022).
32. Patton, H. et al. Deglaciation of the Eurasian ice sheet complex. *Quat. Sci. Rev.* **169**, 148–172 (2017).
33. Hodell, D. A. et al. Anatomy of Heinrich Layer 1 and its role in the last deglaciation. *Paleoceanography* **32**, 284–303 (2017).
34. Orvik, K. A. & Niiler, P. Major pathways of Atlantic water in the northern North Atlantic and Nordic Seas toward Arctic. *Geophys. Res. Lett.* **29**, (2002).
35. Hansen, B. & Østerhus, S. North Atlantic–Nordic Seas exchanges. *Prog. Oceanogr.* **45**, 109–208 (2000).
36. CLIMAP Project Members. Seasonal reconstructions of the Earth's surface at the last glacial maximum. *Geological Society of America* Map and Chart Series MC-36 (1981).
37. Blindheim, J. & Østerhus, S. The Nordic Seas, main oceanographic features. *Geophys. Monogr. -Am. Geophys. Union* **158**, 11–37 (2005).
38. Jennings, A., Andrews, J. & Wilson, L. Holocene environmental evolution of the SE Greenland Shelf North and South of the Denmark Strait: Irminger and East Greenland current interactions. *Quat. Sci. Rev.* **30**, 980–998 (2011).
39. Chapman, M. R. & Maslin, M. A. Low-latitude forcing of meridional temperature and salinity gradients in the subpolar North Atlantic and the growth of glacial ice sheets. *Geology* **27**, 875 (1999).
40. Yin, J. et al. Sea surface temperature and salinity variations from the end of Last Glacial Maximum (LGM) to the Holocene in the northern South China Sea. *Palaeogeogr. Palaeoclimatol. Palaeoecol.* **562**, 110102 (2021).
41. Liu, S. et al. Millennial-scale variability of Indian summer monsoon during the last 42 kyr: Evidence based on foraminiferal Mg/Ca and oxygen isotope records from the central Bay of Bengal. *Palaeogeogr. Palaeoclimatol. Palaeoecol.* **562**, 110112 (2021).
42. Dokken, T. M., Nisancioglu, K. H., Li, C., Battisti, D. S. & Kissel, C. Dansgaard-Oeschger cycles: Interactions between ocean and sea ice intrinsic to the Nordic seas. *Paleoceanography* **28**, 491–502 (2013).
43. Ezat, M. M., Rasmussen, T. L. & Groeneveld, J. Persistent intermediate water warming during cold stadials in the southeastern Nordic seas during the past 65 k.y. *Geology* **42**, 663–666 (2014).
44. Rühlemann, C. et al. Intermediate depth warming in the tropical Atlantic related to weakened thermohaline circulation: Combining paleoclimate data and modeling results for the last deglaciation. *Paleoceanography* **19**, (2004).
45. He, C. et al. North Atlantic subsurface temperature response controlled by effective freshwater input in "Heinrich" events. *Earth Planet. Sci. Lett.* **539**, 116247 (2020).
46. Polyakov, I. V. et al. Greater role for Atlantic inflows on sea-ice loss in the Eurasian Basin of the Arctic. *Ocean. Sci.* **356**, 285–291 (2017).
47. Polyakov, I. V. et al. Weakening of cold halocline layer exposes sea ice to oceanic heat in the Eastern Arctic Ocean. *J. Clim.* **33**, 8107–8123 (2020).
48. Peck, V. L., Hall, I. R., Zahn, R. & Elderfield, H. Millennial-scale surface and subsurface paleothermometry from the northeast Atlantic, 55–8 ka BP. *Paleoceanography* **23**, (2008).
49. Sarnthein, M. et al. Variations in Atlantic surface ocean paleoceanography, 50°-80°N: A time-slice record of the last 30,000 years. *Paleoceanography* **10**, 1063–1094 (1995).
50. Rørvik, K., Rasmussen, T. L., Hald, M. & Husum, K. Intermediate water ventilation in the Nordic seas during MIS 2. *Geophys. Res. Lett.* **40**, 1805–1810 (2013).
51. Rigual-Hernández, A. S. et al. Svalbard ice-sheet decay after the Last Glacial Maximum: New insights from micropalaeontological and organic biomarker paleoceanographical reconstructions. *Palaeogeogr. Palaeoclimatol. Palaeoecol.* **465**, 225–236 (2017).
52. Ezat, M. M. et al. Ventilation history of Nordic Seas overflows during the last (de)glacial period revealed by species-specific benthic foraminiferal ^{14}C dates. *Paleoceanography* **32**, 172–181 (2017).
53. Lind, S., Ingvaldsen, R. B. & Furevik, T. Arctic warming hotspot in the northern Barents Sea linked to declining sea-ice import. *Nat. Clim. Chang.* **8**, 634–639 (2018).
54. Meland, M. Y., Jansen, E. & Elderfield, H. Constraints on SST estimates for the northern North Atlantic/Nordic Seas during the LGM. *Quat. Sci. Rev.* **24**, 835–852 (2005).
55. Hoff, U., Rasmussen, T. L., Stein, R., Ezat, M. M. & Fahl, K. Sea ice and millennial-scale climate variability in the Nordic seas 90 kyr ago to present. *Nat. Commun.* **7**, 12247 (2016).
56. Laskar, J. et al. A long-term numerical solution for the insolation quantities of the Earth. *Astron. Astrophys.* **428**, 261–285 (2004).
57. Tzedakis, P. C., Crucifix, M., Mitsui, T. & Wolff, E. W. A simple rule to determine which insolation cycles lead to interglacials. *Nature* **542**, 427–432 (2017).
58. Alley, R. B. & Clark, P. U. The deglaciation of the Northern Hemisphere: a global perspective. *Annu. Rev. Earth Planet. Sci.* **27**, 149–182 (1999).
59. Jiang, H. et al. Solar forcing of Holocene summer sea-surface temperatures in the northern North Atlantic. *Geology* **43**, 203–206 (2015).
60. Byrkjedal, Ø, Kvamstø, N. G., Meland, M. & Jansen, E. Sensitivity of last glacial maximum climate to sea ice conditions in the Nordic Seas. *Clim. Dyn.* **26**, 473–487 (2006).
61. Calov, R. et al. Transient simulation of the last glacial inception. Part II: sensitivity and feedback analysis. *Clim. Dyn.* **24**, 563–576 (2005).
62. Peixóto, J. P. & Oort, A. H. Physics of climate. *Rev. Mod. Phys.* **56**, 365–429 (1984).
63. Jain, S., Lall, U. & Mann, M. E. Seasonality and Interannual Variations of Northern Hemisphere Temperature: Equator-to-Pole Gradient and Ocean–Land Contrast. *J. Clim.* **12**, 1086–1100 (1999).
64. Rind, D. Latitudinal temperature gradients and climate change. *J. Geophys. Res. Atmos.* **103**, 5943–5971 (1998).
65. Raymo, M. E. & Nisancioglu, K. H. The 41 kyr world: Milankovitch's other unsolved mystery. *Paleoceanography* **18**, 1–6 (2003).
66. Liu, Z. et al. Younger Dryas cooling and the Greenland climate response to CO_2. *Proc. Natl. Acad. Sci.* **109**, 11101–11104 (2012).
67. Häkkinen, S. & Rhines, P. B. Decline of Subpolar North Atlantic Circulation During the 1990s. *Science*. **304**, 555–559 (2004).

68. Moffa-Sánchez, P., Born, A., Hall, I. R., Thornalley, D. J. R. & Barker, S. Solar forcing of North Atlantic surface temperature and salinity over the past millennium. *Nat. Geosci.* **7**, 275–278 (2014).
69. Hewitt, C. D., Broccoli, A. J., Mitchell, J. F. B. & Stouffer, R. J. A coupled model study of the Last Glacial Maximum: Was part of the North Atlantic relatively warm? *Geophys. Res. Lett.* **28**, 1571–1574 (2001).
70. Delworth, T. L. et al. The North Atlantic Oscillation as a driver of rapid climate change in the Northern Hemisphere. *Nat. Geosci.* **9**, 509–512 (2016).
71. Dai, H., Zhao, J., Zhao, W., Huang, H. & Liu, Y. Role of Vertical Mixing in the Upper Ocean in the Seasonal Variation of Arctic Amplification. *J. Geophys. Res.: Atmos.* **127**, 1–15 (2022).
72. Bond, G. et al. Evidence for massive discharges of icebergs into the North Atlantic ocean during the last glacial period. *Nature* **360**, 245–249 (1992).
73. Mikolajewicz, U. et al. Deglaciation and abrupt events in a coupled comprehensive atmosphere–ocean–ice-sheet–solid-earth model. *Climate* **21**, 719–751 (2025).
74. Clark, C. D., Hughes, A. L. C., Greenwood, S. L., Jordan, C. & Sejrup, H. P. Pattern and timing of retreat of the last British-Irish Ice Sheet. *Quat. Sci. Rev.* **44**, 112–146 (2012).
75. Toucanne, S. et al. The first estimation of Fleuve Manche palaeoriver discharge during the last deglaciation: Evidence for Fennoscandian ice sheet meltwater flow in the English Channel ca 20–18 ka ago. *Earth Planet. Sci. Lett.* **290**, 459–473 (2010).
76. Toucanne, S. et al. Millennial-scale fluctuations of the European Ice Sheet at the end of the last glacial, and their potential impact on global climate. *Quat. Sci. Rev.* **123**, 113–133 (2015).
77. Becker, L. W. M., Sejrup, H. P., Hjelstuen, B. O., Haflidason, H. & Dokken, T. M. Ocean-ice sheet interaction along the SE Nordic Seas margin from 35 to 15 ka BP. *Mar. Geol.* **402**, 99–117 (2018).
78. Rørvik, K.-L., Laberg, J. S., Hald, M., Ravna, E. K. & Vorren, T. O. Behavior of the northwestern part of the Fennoscandian Ice Sheet during the Last Glacial Maximum – a response to external forcing. *Quat. Sci. Rev.* **29**, 2224–2237 (2010).
79. Winsborrow, M. C. M., Andreassen, K., Corner, G. D. & Laberg, J. S. Deglaciation of a marine-based ice sheet: Late Weichselian palaeo-ice dynamics and retreat in the southern Barents Sea reconstructed from onshore and offshore glacial geomorphology. *Quat. Sci. Rev.* **29**, 424–442 (2010).
80. Petrini, M. et al. Simulated last deglaciation of the Barents Sea Ice Sheet primarily driven by oceanic conditions. *Quat. Sci. Rev.* **238**, 106314 (2020).
81. Petrini, M. et al. Interplay of grounding-line dynamics and sub-shelf melting during retreat of the Bjørnøyrenna Ice Stream. *Sci. Rep.* **8**, 7196 (2018).
82. van Aalderen, V., Charbit, S., Dumas, C. & Quiquet, A. Relative importance of the mechanisms triggering the Eurasian ice sheet deglaciation in the GRISLI2.0 ice sheet model. *Climate* **20**, 187–209 (2024).
83. Osman, M. B. et al. Globally resolved surface temperatures since the Last Glacial Maximum. *Nature* **599**, 239–244 (2021).
84. McManus, J. F., Francois, R., Gherardi, J.-M., Keigwin, L. D. & Brown-Leger, S. Collapse and rapid resumption of Atlantic meridional circulation linked to deglacial climate changes. *Nature* **428**, 834–837 (2004).
85. Lippold, J. et al. Does sedimentary ^{231}Pa/^{230}Th from the Bermuda Rise monitor past Atlantic Meridional Overturning Circulation? *Geophys. Res. Lett.* **36**, (2009).
86. Hemming, S. R. Heinrich events: Massive late Pleistocene detritus layers of the North Atlantic and their global climate imprint. *Rev. Geophys.* **42**, (2004).
87. Bond, G. C. & Lotti, R. Iceberg Discharges into the North Atlantic on Millennial Time Scales During the Last Glaciation. *Science* **267**, 1005–1010 (1995).
88. Marcott, S. A. et al. Ice-shelf collapse from subsurface warming as a trigger for Heinrich events. *Proc. Natl. Acad. Sci.* **108**, 13415–13419 (2011).
89. Deaney, E. L., Barker, S. & van de Flierdt, T. Timing and nature of AMOC recovery across Termination 2 and magnitude of deglacial CO2 change. *Nat. Commun.* **8**, 14595 (2017).
90. Bauska, T. K., Marcott, S. A. & Brook, E. J. Abrupt changes in the global carbon cycle during the last glacial period. *Nat. Geosci.* **14**, 91–96 (2021).
91. Schmitt, J. et al. Carbon Isotope constraints on the deglacial CO_2 rise from ice cores. *Science* **336**, 711–714 (2012).
92. Blaauw, M. & Christen, J. A. Flexible paleoclimate age-depth models using an autoregressive gamma process. *Bayesian Anal.* **6**, 457–474 (2011).
93. Heaton, T. J. et al. Marine20—The Marine Radiocarbon Age Calibration Curve (0–55,000 cal BP). *Radiocarbon* **62**, 779–820 (2020).
94. Heaton, T. J. et al. Marine radiocarbon calibration in polar regions: A simple approximate approach using marine20. *Radiocarbon* **65**, 848–875 (2023).
95. Ownsworth, E. et al. Tracking sediment delivery to central Baffin Bay during the past 40 kyrs: Insights from a multiproxy approach and new age model. *Quat. Sci. Rev.* **308**, 108082 (2023).
96. Pak, D. K., Lea, D. W. & Kennett, J. P. Seasonal and interannual variation in Santa Barbara Basin water temperatures observed in sediment trap foraminiferal Mg/Ca. *Geochem. Geophys. Geosyst.* **5**, (2004).
97. Pearce, N. J. G. et al. A compilation of new and published major and trace element data for NIST SRM 610 and NIST SRM 612 Glass Reference Materials. *Geostand. Newsl.* **21**, 115–144 (1997).
98. Holland, K., Eggins, S. M., Hönisch, B., Haynes, L. L. & Branson, O. Calcification rate and shell chemistry response of the planktic foraminifer Orbulina universa to changes in microenvironment seawater carbonate chemistry. *Earth Planet. Sci. Lett.* **464**, 124–134 (2017).
99. Liu, Y. et al. In situ analysis of major and trace elements of anhydrous minerals by LA-ICP-MS without applying an internal standard. *Chem. Geol.* **257**, 34–43 (2008).
100. Chen, L. et al. Accurate determinations of fifty-four major and trace elements in carbonate by LA–ICP-MS using normalization strategy of bulk components as 100%. *Chem. Geol.* **284**, 283–295 (2011).
101. Rosenthal, Y., Field, M. P. & Sherrell, R. M. Precise determination of element/calcium ratios in calcareous samples using sector field inductively coupled plasma mass spectrometry. *Anal. Chem.* **71**, 3248–3253 (1999).
102. Evans, D., Brierley, C., Raymo, M. E., Erez, J. & Müller, W. Planktic foraminifera shell chemistry response to seawater chemistry: Pliocene–Pleistocene seawater Mg/Ca, temperature and sea level change. *Earth Planet. Sci. Lett.* **438**, 139–148 (2016).
103. Russell, A. D., Hönisch, B., Spero, H. J. & Lea, D. W. Effects of seawater carbonate ion concentration and temperature on shell U, Mg, and Sr in cultured planktonic foraminifera. *Geochim. Cosmochim. Acta* **68**, 4347–4361 (2004).
104. Morley, A. et al. A solution for constraining past marine Polar Amplification. *Nat. Commun.* **15**, 9002 (2024).
105. Jonkers, L., Jiménez-Amat, P., Mortyn, P. G. & Brummer, G.-J. A. Seasonal Mg/Ca variability of N. pachyderma (s) and G. bulloides: Implications for seawater temperature reconstruction. *Earth Planet. Sci. Lett.* **376**, 137–144 (2013).

106. Locarnini, R. A. et al. World Ocean Atlas 2023, Volume 1: Temperature. http://repository.library.noaa.gov/view/noaa/60599 https://doi.org/10.25923/54bh-1613 (2024).
107. Shackleton, N. J. Attainment of isotopic equilibrium between ocean water and the benthonic foraminifera geuns Uvigerina: Isotopic changes in the ocean during the last glacial. *Colloq. Int. C. N. R. S.* **219**, 203–210 (1974).
108. O'Neil, J. R., Clayton, R. N. & Mayeda, T. K. Oxygen Isotope Fractionation in Divalent Metal Carbonates. *J. Chem. Phys.* **51**, 5547–5558 (1969).
109. Simstich, J., Sarnthein, M. & Erlenkeuser, H. Paired δ18O signals of Neogloboquadrina pachyderma (s) and Turborotalita quinqueloba show thermal stratification structure in the Nordic Seas. *Mar. Micropaleontol.* **48**, 107–125 (2003).
110. Adkins, J. F., McIntyre, K. & Schrag, D. P. The Salinity, Temperature, and $\delta^{18}O$ of the Glacial Deep Ocean. *Science* **298**, 1769–1773 (2002).
111. Thirumalai, K., Quinn, T. M. & Marino, G. Constraining past seawater $\delta^{18}O$ and temperature records developed from foraminiferal geochemistry. *Paleoceanography* **31**, 1409–1422 (2016).
112. Davis, C. V., Fehrenbacher, J. S., Hill, T. M., Russell, A. D. & Spero, H. J. Relationships Between Temperature, pH, and Crusting on Mg/Ca Ratios in Laboratory-Grown Neogloboquadrina Foraminifera. *Paleoceanography* **32**, 1137–1152 (2017).
113. Hupp, B. N. & Fehrenbacher, J. S. Geochemical differences between alive, uncrusted and dead, crusted shells of neogloboquadrina pachyderma: implications for paleoreconstruction. *Paleoceanogr. Paleoclimatol.* **38**, 1–19 (2023).
114. Otto-Bliesner, B. L. et al. Climate sensitivity of moderate- and low-resolution versions of CCSM3 to preindustrial forcings. *J. Clim.* **19**, 2567–2583 (2006).
115. Collins, W. D. et al. The Community Climate System Model Version 3 (CCSM3). *J. Clim.* **19**, 2122–2143 (2006).
116. Yeager, S. G., Shields, C. A., Large, W. G. & Hack, J. J. The Low-Resolution CCSM3. *J. Clim.* **19**, 2545–2566 (2006).
117. He, C. et al. Hydroclimate footprint of pan-Asian monsoon water isotope during the last deglaciation. *Sci. Adv.* **7**, 1–11 (2021).
118. Dong W.& Liu Y. Dataset for "Insolation-forced oceanic changes: key trigger of the Eurasian Ice Sheet collapse and the Last Termination". Figshare. Dataset, https://doi.org/10.6084/m9.figshare.30536837 (2026).
119. Bauch, H. A. et al. A multiproxy reconstruction of the evolution of deep and surface waters in the subarctic Nordic seas over the last 30,000 yr. *Quat. Sci. Rev.* **20**, 659–678 (2001).
120. Valdimarsson, H. & Malmberg, S.-A. Near-surface circulation in Icelandic waters derived from satellite tracked drifters. *Rit Fiskideild* **16**, 23–39 (1999).
121. RUDDIMAN, W. F. Late Quaternary deposition of ice-rafted sand in the subpolar North Atlantic (lat 40° to 65°N). *Geol. Soc. Am. Bull.* **88**, 1813 (1977).
122. North Greenland Ice Core Project Members High-resolution record of Northern Hemisphere climate extending into the last interglacial period. *Nature* **431**, 147–151 (2004).
123. Rasmussen, S. O. et al. A new Greenland ice core chronology for the last glacial termination. *J. Geophys. Res.: Atmos.* **111**, (2006).
124. Kindler, P. et al. Temperature reconstruction from 10 to 120 kyr b2k from the NGRIP ice core. *Climate* **10**, 887–902 (2014).
125. Broecker, W., Bond, G., Klas, M., Clark, E. & McManus, J. Origin of the northern Atlantic's Heinrich events. *Clim. Dyn.* **6**, 265–273 (1992).
126. Peltier, W. R. & Fairbanks, R. G. Global glacial ice volume and Last Glacial Maximum duration from an extended Barbados sea level record. *Quat. Sci. Rev.* **25**, 3322–3337 (2006).
127. Yokoyama, Y., Lambeck, K., De Deckker, P., Johnston, P. & Fifield, L. K. Timing of the Last Glacial Maximum from observed sea-level minima. *Nature* **406**, 713–716 (2000).
128. Yokoyama, Y., De Deckker, P., Lambeck, K., Johnston, P. & Fifield, L. K. Sea-level at the Last Glacial Maximum: evidence from northwestern Australia to constrain ice volumes for oxygen isotope stage 2. *Palaeogeogr. Palaeoclimatol. Palaeoecol.* **165**, 281–297 (2001).
129. Bard, E. et al. Deglacial sea-level record from Tahiti corals and the timing of global meltwater discharge. *Nature* **382**, 241–244 (1996).
130. Deschamps, P. et al. Ice-sheet collapse and sea-level rise at the Bølling warming 14,600 years ago. *Nature* **483**, 559–564 (2012).
131. Hanebuth, T., Stattegger, K. & Grootes, P. M. Rapid Flooding of the Sunda Shelf: A Late-Glacial Sea-Level Record. *Science* **288**, 1033–1035 (2000).
132. Rasmussen, T. L., Thomsen, E., van Weering, T. C. E. & Labeyrie, L. Rapid changes in surface and deep water conditions at the Faeroe Margin during the last 58,000 years. *Paleoceanography* **11**, 757–771 (1996).

Acknowledgements
We thank the crew of icebreaker Xuelong for assistance in retrieving the sediment core. We thank Yan Zhang (First Institute of Oceanography, MNR) for her technical assistance of LA-ICP-MS. We thank Yi Zhong (Southern University of Science and Technology) for reading the early version of the manuscript.

Author contributions
D.W., Y.L., and X.Z. designed the study; Y.L. sampled the core; W.D. constructed the age model, prepared and analyzed $\delta^{18}O$ data, performed the LA-ICP-MS test, and drafted the original manuscript; S.L. and X.Z. contributed to the model simulation results; D.F. contributed substantially to all aspects; J.E., E.R.G., Y.R., and N.H. were responsible for the evaluation and quality control. D.W., Y.L., X.Z., S.L., J.E., E.R.G., Y.R., N.H., and D.F. contributed to the interpretation and the final manuscript.

Funding
Y.L. discloses support for the research and publication of this work from the National Key Research and Development Program of China (Grant No. 2023YFF0804600). X.Z. discloses support for the research of this work from the National Key Research and Development Program of China (Grant No. 2023YFF0805200). N.H. discloses support for the research of this work from the National Natural Science Foundation of China (Grant nos. 42076079 and 41676053).

Competing interests
The authors declare no competing interests.

Additional information
Supplementary information The online version contains supplementary material available at https://doi.org/10.1038/s41467-026-73152-7.

Correspondence and requests for materials should be addressed to Yanguang Liu or Xu Zhang.

Peer review information *Nature Communications* thanks Michele Petrini, who co-reviewed with Karlijn PloegJorge Alvarez-Solas, Audrey Morleyand, and Victor van Aalderen for their contribution to the peer review of this work. A peer review file is available.

https://doi.org/10.1038/s41467-026-73152-7